



Article

An Approach to Predicting Urban Carbon Stock Using a Self-Attention Convolutional Long Short-Term Memory Network Model: A Case Study in Wuhan Urban Circle

Zhi Zhou¹, Xueling Wu^{1,2,*}  and Bo Peng¹ 

¹ School of Geophysics and Geomatics, China University of Geosciences, Wuhan 430074, China; zzhou@cug.edu.cn (Z.Z.); plumbumer@cug.edu.cn (B.P.)

² Key Laboratory of Urban Land Resources Monitoring and Simulation, Ministry of Natural Resources, Shenzhen 518034, China

* Correspondence: wuxl@cug.edu.cn

Abstract: To achieve the regional goal of “double carbon”, it is necessary to map the carbon stock prediction for a wide area accurately and in a timely fashion. This paper introduces a long- and short-term memory network algorithm called the Self-Attention Convolutional Long and Short-Term Memory Network (SA-ConvLSTM). This paper takes the Wuhan urban circle of China as the research object, establishes a carbon stock AI prediction model, constructs a carbon stock change evaluation system, and investigates the correlation between carbon stock change and land use change during urban expansion. The results demonstrate that (1) the overall accuracy of the ConvLSTM and SA-ConvLSTM models improved by 4.68% and 4.70%, respectively, when compared to the traditional metacellular automata prediction methods (OS-CA, Open Space Cellular Automata Model), and for small sample categories such as barren land, shrubs, and grassland, the accuracy of SA-ConvLSTM increased by 17.15%, 43.12%, and 51.37%, respectively; (2) from 1999 to 2018, the carbon stock in the Wuhan urban area showed a decreasing trend, with an overall decrease of 6.49×10^6 MgC. The encroachment of arable land due to rapid urbanization is the main reason for the decrease in carbon stock in the Wuhan urban area. From 2018 to 2023, the predicted value of carbon stock in the Wuhan urban area was expected to increase by 9.17×10^4 MgC, mainly due to the conversion of water bodies into arable land, followed by the return of cropland to forest; (3) the historical spatial error model (SEM) indicates that for each unit decrease in carbon stock change, the Single Land Use Dynamic Degree (SLUDD) of water bodies and impervious surfaces will increase by 119 and 33 units, respectively. For forests, grasslands, and water bodies, the future spatial error model (SEM) indicated that for each unit increase in carbon stock change, the SLUDD would increase by 55, 7, and -305 units, respectively. This study demonstrates that we can use deep neural networks as a new method for predicting land use expansion, revealing the key impacts of land use change on carbon stock change from both historical and future perspectives and providing valuable insights for policymakers.

Keywords: carbon stock; InVEST model; LULC spatial–temporal prediction; spatial lag and error model; SA-ConvLSTM model



Citation: Zhou, Z.; Wu, X.; Peng, B. An Approach to Predicting Urban Carbon Stock Using a Self-Attention Convolutional Long Short-Term Memory Network Model: A Case Study in Wuhan Urban Circle. *Remote Sens.* **2024**, *16*, 4372. <https://doi.org/10.3390/rs16234372>

Academic Editors: Tong Li and Yash Dang

Received: 12 September 2024

Revised: 13 November 2024

Accepted: 14 November 2024

Published: 22 November 2024



Copyright: © 2024 by the authors. Licensee MDPI, Basel, Switzerland. This article is an open access article distributed under the terms and conditions of the Creative Commons Attribution (CC BY) license (<https://creativecommons.org/licenses/by/4.0/>).

1. Introduction

The carbon stock in urban land use is a fundamental component of the carbon cycle in urban ecosystems [1], playing a critical role in regulating climate change, safeguarding ecosystem health, and understanding the environmental dynamics of cities [2]. Nevertheless, changes in carbon stocks due to human activities such as urbanization have become increasingly significant in international environmental research, particularly given the rapid expansion of urban areas and their impact on carbon dynamics [3–6]. Urban soil organic carbon is a significant constituent of carbon stocks that are directly influenced by

land use practices within city environments [7]. Numerous factors influence the quantity and distribution of urban organic carbon, including meteorological conditions, urban land use practices, and the variety of plant species in city environments [8–10]. It is crucial to have precise estimations and predictions of urban land-use-related carbon stocks, particularly in light of the escalating consequences of climate change on densely populated areas. The majority of conventional approaches to monitoring urban soil carbon stocks rely on sampling and field surveys, which are often constrained by their limited temporal and spatial coverage in city environments [11–13]. To ensure a timely and comprehensive understanding of carbon stock fluctuations in urban areas, sophisticated remote sensing instruments and data processing tools are essential [14]. The utilization of satellite remote sensing technology has transformed remotely sensed data into a crucial instrument for examining urban carbon stocks associated with land use changes [15]. Satellite observations provide a diverse array of accurate data with significant temporal and spatial precision, crucial for enhancing the surveillance of urban soil organic carbon stocks across various city ecosystems [16]. In comparison to conventional methods, remote sensing offers numerous benefits for urban environments, such as cost-effectiveness, extensive coverage, and real-time data acquisition [17]. The investigation of urban carbon stocks through the implementation of machine learning models, particularly deep learning, has gained significant attention in the scientific community, highlighting advancements in analyzing complex urban ecosystems. For example, Zhang et al. [18] utilized the radial basis function (RF) method along with remote sensing data from Landsat TM and OLI satellites to estimate the spatial and temporal distribution of carbon stocks in urban forests in the Hangjiahu region.

Current research on predicting urban carbon stocks frequently employs land use simulations alongside carbon stock estimation models, often involving complex models and varied data sources [19]. Early methodologies for urban carbon stock assessment primarily included field sampling techniques, computational methods [20], remote sensing-based estimation methods, and model-based approaches. Various research domains, including urban ecological regions, diverse urban land use categories, and extensive municipal and provincial levels, have implemented these techniques. A substantial body of research, including studies by Leh et al. [21], He et al. [22], Babbar et al. [23], and Wang et al. [24] have provided significant evidence supporting the widespread application of the InVEST model in these urban settings. In contrast to other models, the InVEST model demonstrates superior output capability with reduced input requirements, making it especially effective for urban carbon stock assessments [25]. Furthermore, the multilevel design of the InVEST model, comprising numerous modules, makes it particularly suitable for examination across various urban dimensions and contexts. The model can expedite the computation of urban carbon stocks and is ideally suited for large-scale assessments in metropolitan areas. Subsequently, researchers have increasingly focused on estimating forthcoming urban carbon stocks. Commonly used models in these urban studies include CA-Markov [26], FLUS [27,28], Clue-s [29], and PLUS [30–32]. Nevertheless, in urban applications, the ability of cellular automata-based prediction methods to integrate temporal information from time-series data with global contextual information in spatial analysis is somewhat limited. To address these issues, our study employs deep learning algorithms and satellite remote sensing data to accurately estimate and predict carbon stocks associated with urban land use in the Wuhan urban circle [33]. By integrating urban-specific data types such as meteorology, soil, and vegetation, our study analyzes and explores the correlation between carbon stocks generated by urban land use and the various factors influencing these stocks. The core methodology for predicting urban carbon stocks in this paper is structured in two steps. The first step involves predicting future urban land use, and the second step estimates carbon stocks based on these predicted land use scenarios in the Wuhan urban circle.

In this study, we utilized land use data from the Wuhan urban area spanning from 1999 to 2019. Both traditional cellular automata models and deep learning techniques were employed to simulate and forecast land use patterns for the period from 2019 to 2023. Additionally, this research explores the effectiveness of deep learning methods

in simulating and predicting land use changes. Subsequently, we calculated the carbon stock from 1999 to 2023 using the InVEST model and analyzed the spatial and temporal variations in carbon stock within the Wuhan urban area. Finally, the relationships among three indicators—SLUDD, LC, and LUM—and their impact on carbon stock changes were investigated using the spatial error model (SEM) and the spatial lag model (SLM). The innovation of this study lies in the proposed prediction method for estimating carbon stock, utilizing the SA-ConvLSTM model [34], which differs significantly from existing methods. This approach not only predicts carbon stock changes but also examines the relationship between land use and carbon stock variations.

The remainder of this paper is organized as follows. Section 2 presents the theoretical framework. Section 3 details the study area, research methodology, and data sources. Section 4 discusses the analysis of the results. Section 5 provides a discussion of these findings, and these are followed by the Conclusion.

2. Theoretical Framework

The flowchart in Figure 1 illustrates our innovative approach to predicting and analyzing carbon stocks. It is structured into four main components: data preparation, a deep learning-based land use prediction framework, spatio-temporal prediction of carbon stock, and correlation analysis between carbon stock and land use. In this paper, we employ a combination of AI technology and GIS spatial analysis to construct an AI prediction model for carbon stock, develop an evaluation system for monitoring carbon stock changes, and comprehensively analyze the linkage between carbon stock changes and land use changes during urban expansion. This study provides a reference for mapping the carbon stock background and offers guidance for government agencies to formulate future land planning strategies aimed at achieving the dual-carbon goal promptly.

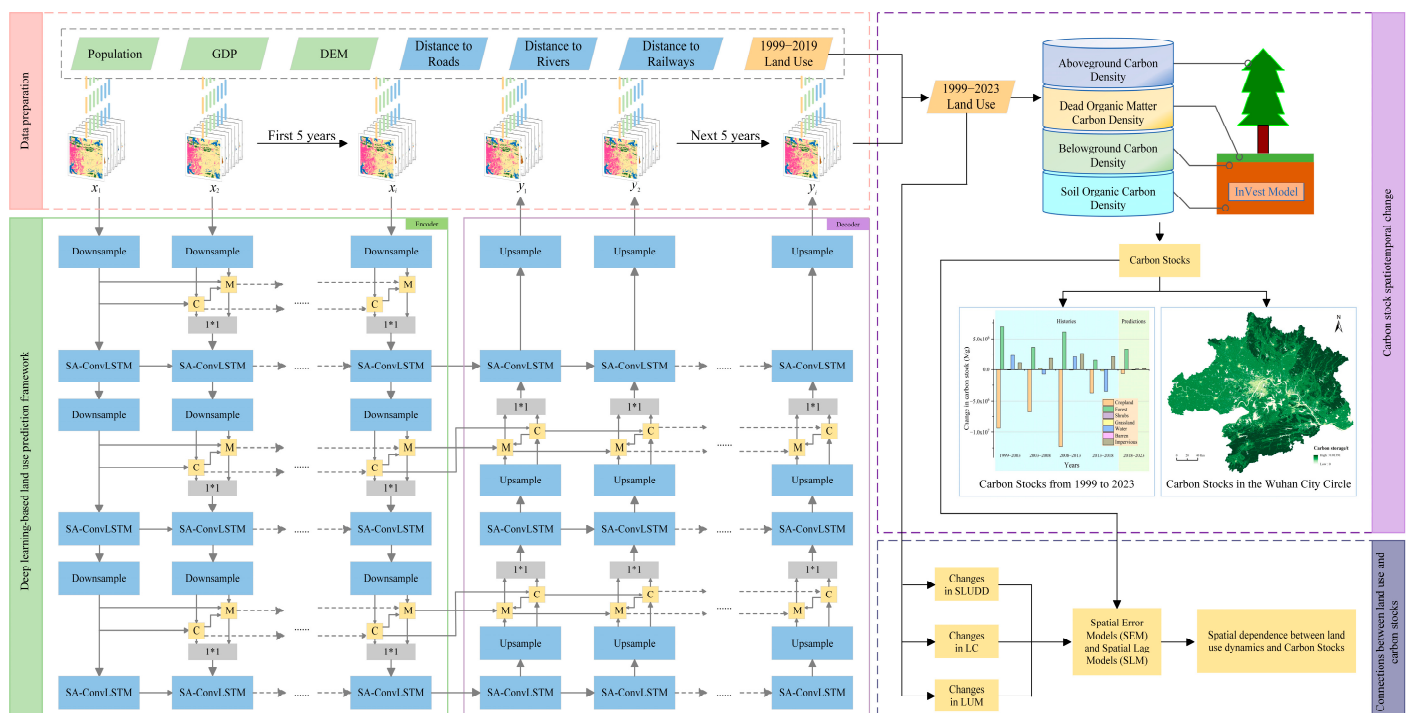


Figure 1. Flowchart for predicting and analyzing urban carbon stocks.

3. Materials and Methodology

3.1. Study Area

The Wuhan City Circle [35] is located in the central region of Hubei Province, China (Figure 2), and serves as both the central hub and the capital of the province. The Wuhan City Circle is located in a subtropical monsoon climatic zone characterized by well-defined

seasons. Summer is characterized by high temperatures and humidity and the majority of the annual precipitation, while winter features comparatively low temperatures. Spring and autumn, on the other hand, are characterized by mild and pleasant weather. Wuhan is located in the Jiangnan Plain, encircled by hills and mountains, with rivers such as the Han River and Yangtze River flowing through it (Figure 2). This geographical configuration significantly influences the city's transit infrastructure and water use. Over the past two decades, Wuhan has experienced significant infrastructure development, encompassing transportation, water management, and urban construction.

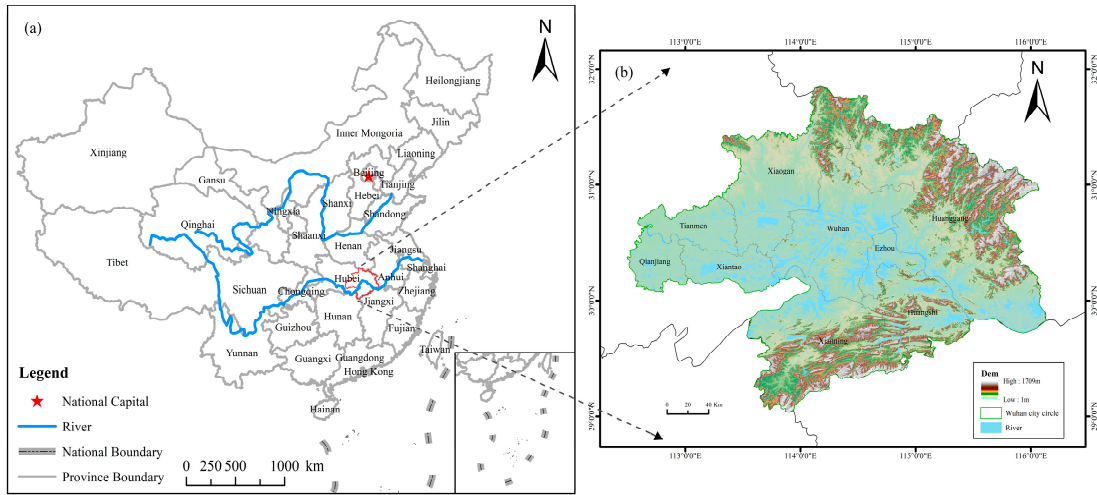


Figure 2. (a) The geographical position of the Wuhan City Circle in China; (b) The Digital Elevation Model (DEM) of the Wuhan City Circle.

3.2. Methodology

3.2.1. Predicting Land Use Based on SA-ConvLSTM Modeling SA-ConvLSTM Model

This study employs the encoder–decoder architecture to accurately forecast spatio-temporal sequences by capturing both spatial and temporal characteristics of the input data through machine learning [36]. The encoder module of the model comprises three downsampling layers and three Self-Attention Convolutional Long Short-Term Memory Network [34] (SA-ConvLSTM) layers. The downsampling layer reduces the image size through methods such as max pooling, average pooling, or strided convolution to extract important spatial features [37]. In accordance with the common time intervals used in urban planning in China [38], the model framework is designed to use the previous 5 years to predict changes in the subsequent 5 years. ConvLSTM effectively models both the geographical information and the spatio-temporal elements contained in the time series. The Spatial Attention Mechanism (SAM) enhances the model's long-term memory by storing and utilizing both temporal and spatial information [39].

The model is formulated as follows:

$$\hat{\mathcal{X}}_t = SA(\mathcal{X}_t), \hat{\mathcal{H}}_{t-1} = SA(\mathcal{H}_{t-1}) \quad (1)$$

$$i_t = \sigma(W_{xi} * \hat{\mathcal{X}}_t + W_{hi} * \hat{\mathcal{H}}_{t-1} + b_i) \quad (2)$$

$$f_t = \sigma(W_{xf} * \hat{\mathcal{X}}_t + W_{hf} * \hat{\mathcal{H}}_{t-1} + b_f) \quad (3)$$

$$g_t = \tanh(W_{xc} * \hat{\mathcal{X}}_t + W_{hc} * \hat{\mathcal{H}}_{t-1} + b_c) \quad (4)$$

$$C_t = f_t \circ C_{t-1} + i_t \circ g_t \quad (5)$$

$$o_t = \sigma(W_{xo} * \hat{\mathcal{X}}_t + W_{ho} * \hat{\mathcal{H}}_{t-1} + b_o) \quad (6)$$

$$\mathcal{H}_t = o_t \circ \tanh(C_t) \tag{7}$$

SA is an abbreviation for the self-attention module algorithm. Implementing the self-attention module on the input $\widehat{\mathcal{X}}_t$ at time step t yields the result \mathcal{X}_t . The model captures input sequence interdependencies using the self-attention module. The result is acquired by applying the self-attention module on the hidden state $\widehat{\mathcal{H}}_{t-1}$ from the previous time step. It helps the model capture hidden state internal linkages. i_t represents the input gate. The sigmoid function (σ) determines the new state magnitude, which controls the addition of fresh information g_t to the cell state C_t . The forgetting gate is f_t . A sigmoid function controls the forgetting gate such that information from the previous time step cell state C_{t-1} is maintained in the current time step. The hyperbolic tangent (\tanh) function processes g_t , which contains additional information. It calculates the value to add to C_t , a candidate cell state. Variable C_t denotes cell state. Input data are stored in the LSTM cell's memory. With g_t , the forgetting gate f_t controls the assimilation of new information and the retention and omission of information from the previous time step's cell state. The output gate is o_t . A sigmoid function determines the cell state C_t , which is provided to the hidden state \mathcal{H}_t . At time step t , H is the concealed state. This is the LSTM cell's main output. The cell state C_t is multiplied by the output gate o_t and processed using a hyperbolic tangent function. The altered input sequences and prior hidden states are linearly combined using the weight matrices $W_{xi}, W_{xf}, W_{xc}, W_{xo}, W_{hi}, W_{hf}, W_{hc},$ and W_{ho} . This calculation calculates input gates, oblivion gates, candidate cell state values, and output gates. Training generates weight matrices as model parameters. The bias variables $b_I, b_f, b_c,$ and b_o fine-tune gate behavior and the computation of the candidate cell state [34].

The model data can be categorized into two types: computational self-attention and ConvLSTM operations, as shown in Figure 3. The purpose of employing self-attention in data processing is to enhance the ability to retain long-term spatio-temporal information and to boost the capability to learn from data with subtle spatial variations. ConvLSTM [40], a variant of the LSTM architecture, replaces pointwise multiplications with convolutional operations. This allows for the simultaneous learning of spatial and temporal information. Additionally, ConvLSTM incorporates an attention mechanism to selectively focus on important aspects of the data, thereby improving the retention of key information, especially in small samples.

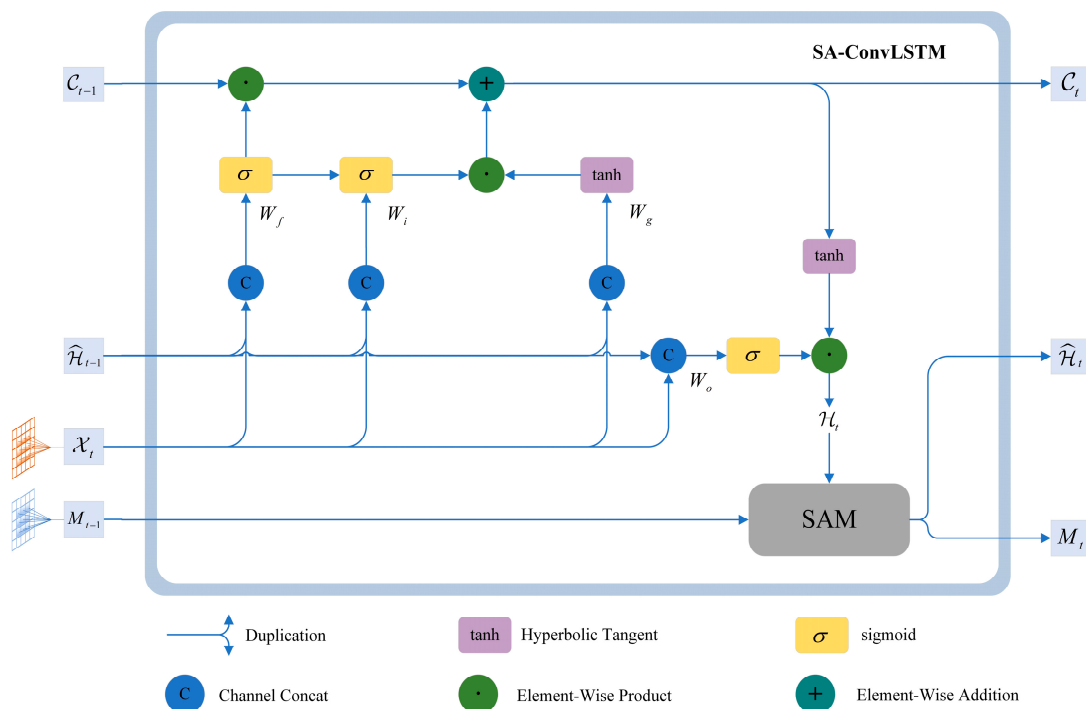


Figure 3. The Self-Attention ConvLSTM block.

SAM Module

The SAM module utilizes a unique memory cell, referred to as M , to contain spatial information that is injected with temporal correlation. The inputs to the SAM module are the ConvLSTM exported hidden layer state, H_t , from the current time step, and the memory view, M_{t-1} , from the previous time step.

As shown in Figure 4, the SA mechanism analyzes the input H_t to generate the characteristic Z_h . This process emphasizes the significance of certain components in H_t . Simultaneously, H_t functions as a query, while M_{t-1} is processed by the attention mechanism to generate the feature Z_m . This highlights the components of H_t that have a distinct reliance on M_{t-1} . By combining the elements Z_h and Z_m , we obtain the composite feature Z , which encompasses data from the present time step and overall temporal memory. Afterward, the combined characteristics Z are connected to the gating mechanism in the LSTM to modify the state of the hidden layer and the memory cells. This function modifies the hidden layer state \widehat{H}_t and the memory M_t of the current time step. The SAM module is structured in the following manner [34]:

$$i'_t = \sigma(W_{m;zi} * Z + W_{m;hi} * H_t + b_{m;i}) \tag{8}$$

$$g'_t = \tanh(W_{m;zg} * Z + W_{m;hg} * H_t + b_{m;g}) \tag{9}$$

$$M_t = (1 - i'_t) \circ M_{t-1} + i'_t \circ g'_t \tag{10}$$

$$o'_t = \sigma(W_{m;zo} * Z + W_{m;ho} * H_t + b_{m;o}) \tag{11}$$

$$\widehat{H}_t = o'_t \circ M_t \tag{12}$$

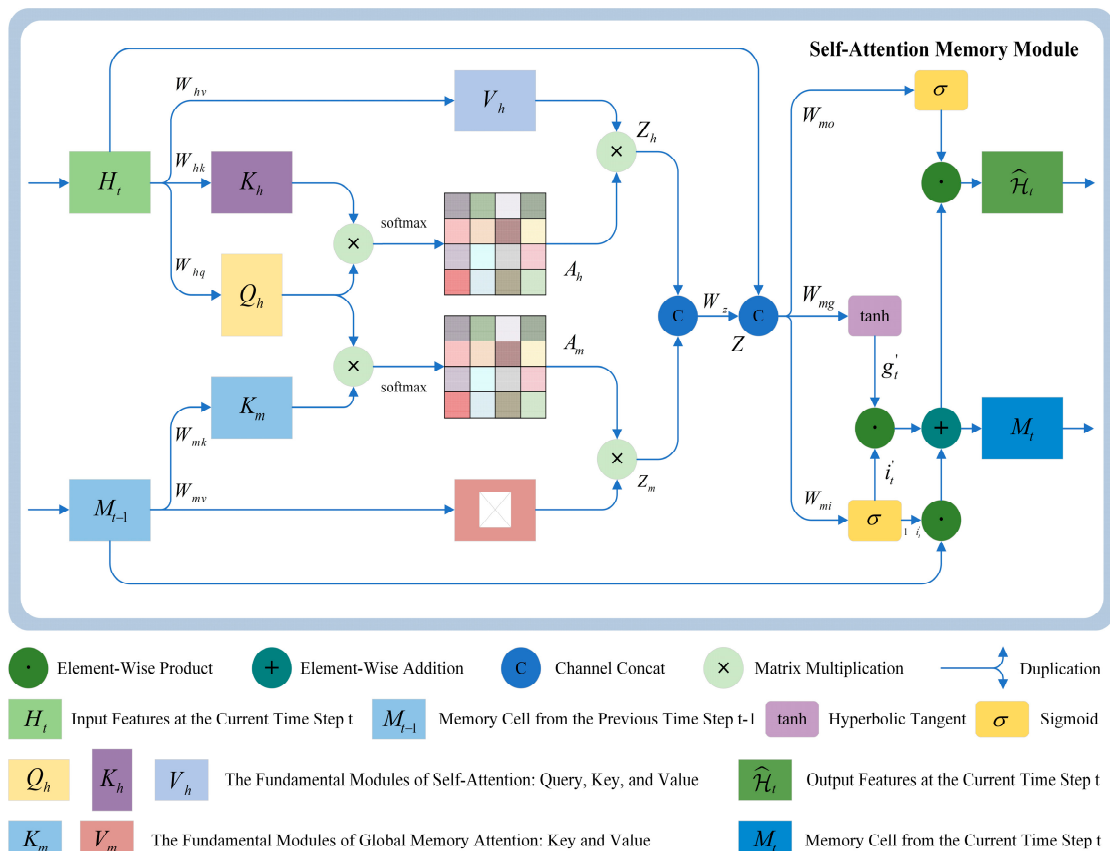


Figure 4. Self-Attention Memory Module.

In the above equation, the symbol i'_t denotes the input gate. The sigmoid function is used to determine the value that controls the quantity of new information, denoted as g'_t , that should be introduced to the existing state. The gating mechanism regulates the amount of past memory that should be preserved in the present time step t . The variable g'_t represents the updated memory candidate obtained by using the hyperbolic tangent function. It denotes the additional data that will be included in the memory M_t . M_t is the model's internal state, which stores input sequence information. The system is updated by the input gate i'_t , the new information g'_t , and the memory gate M_{t-1} forgetting the process from the previous time step. The output gate is denoted as o'_t . The value is transformed using a sigmoid function to regulate the impact of the information stored in memory M_t on the output and the impact it has on the resulting product. The gate mechanism quantifies the impact of the memory gate information on the output value \widehat{H}_t . H_t represents the time step t , which includes the memory gate M_t and the output gate o'_t . This assesses the impact of the stored information on the model's output. The parameters used for managing the gating and the memory update are the weight matrices $W_{m,zi}$, $W_{m,hi}$, $W_{m,hg}$, $W_{m,zg}$, $W_{m,zo}$, $W_{m,ho}$, as well as the bias terms $b_{m,i}$, $b_{m,g}$, and $b_{m,o}$.

3.2.2. Using the InVEST Model to Analyze the Carbon Stock

By immobilizing elemental carbon in soils and plants to control atmospheric carbon levels, carbon storage serves as a crucial ecosystem-regulating function that helps mitigate climate change [41]. The InVEST model is one of the most frequently used tools for estimating carbon stocks in extensive ecosystem assessments [42]. In the carbon stocks module of the InVEST model, ecosystem carbon stocks are categorized into four basic reservoirs: soil carbon (found in organic and mineral soils), dead organic carbon (found in apoplastic material, fallen or standing dead wood), above-ground biomass carbon (found in all living plants above the soil), and below-ground biomass carbon (found in the active root system of plants). Below are the formulae for these reservoirs:

$$C_i = C_{above} + C_{below} + C_{soil} + C_{dead} \quad (13)$$

$$C_{total} = \sum_{i=1}^n C_i \times A_i, (i = 1, 2, \dots, n) \quad (14)$$

C_i represents the carbon density of land use type i (Mg/ha); C_{above} represents the carbon density of above-ground biomass (Mg/ha); C_{below} represents the carbon density of below-ground biomass (Mg/ha); C_{soil} represents the soil carbon density (Mg/ha); C_{dead} represents the carbon density of inorganic matter (Mg/ha); C_{total} represents the total ecosystem carbon stock (Mg/ha), A_i represents the total area of land use type i (hm²), and n is the total number of land use types.

The carbon storage module of the InVEST model operates on the fundamental premise that the carbon density of each land cover type remains consistent. The computation of regional vegetation carbon stocks was achieved by multiplying the fixed carbon density values of various vegetation types by their corresponding geographical areas. Given the significant variability in carbon density among various scholars [43–45], it is advisable to rely on literature that specifically focuses on Hubei Province as a reference [46,47]. To compensate for the lack of data on certain Land Use and Land Cover (LULC) categories, we used the China Terrestrial Ecosystem Carbon Density Dataset [48] and gathered information from similar locations [49]. This allowed us to improve the accuracy of the needed carbon density data. The carbon density of different land use types is shown in Table 1.

Table 1. Carbon intensity of each land use type in the area (Mg/ha).

Land Use Type	Above-Ground Carbon Density	Below-Ground Carbon Density	Soil Organic Carbon Density	Dead Organic Matter Carbon Density	Total Carbon Density
Cropland	16.49	10.89	75.82	2.11	105.31
Forest	30.14	6.03	100.15	2.78	139.1
Shrubs	8.67	4.05	82.9	0.87	96.49
Grassland	14.29	17.15	87.05	7.28	125.77
Water	9.3	14.7	81.7	43.1	148.8
Barren	10.36	2.07	34.42	0.96	47.81
Impervious	7.61	1.52	34.33	0	43.46

The CLCD land use data categorizes rivers and lakes collectively as water bodies without distinguishing between natural water bodies, reservoirs, ponds, tidal flats, and beaches [50]. Considering that wetlands typically store significant amounts of carbon [51], assigning a carbon density of zero to water bodies is inappropriate. Therefore, within the study area, the wetland carbon density coefficient has been adjusted based on the area distribution ratios of rivers and lakes from the CNLUCC data [52]. The CNLUCC land use dataset was obtained from the Institute of Geographic Sciences and Natural Resources Research, China (<http://www.resdc.cn/>, accessed on 12 November 2024). The carbon density coefficient for water bodies is calculated by dividing the average area of lakes, reservoirs, and tidal flats over 20 years by the total water area and then multiplying by the carbon density coefficient for wetlands.

3.2.3. Indicators for the Assessment of Predictive Models

The performance of the multivariate classification model is evaluated using the following metrics. In land use forecasting, it is common to encounter an uneven data distribution, with some categories having fewer samples. If emphasis is placed solely on overall accuracy, the model may perform well in categories with a larger number of samples but exhibit subpar performance in categories with fewer samples. Emphasizing the precision of small data samples is crucial for accurately assessing the model's performance in these critical areas.

$$Accuracy = \frac{TP}{TP + FN + FP} \quad (15)$$

$$Precision = \frac{TP}{TP + FP} \quad (16)$$

$$Recall = \frac{TP}{TP + FN} \quad (17)$$

$$F1 = 2 \times \frac{Precision \times Recall}{Precision + Recall} \quad (18)$$

Accuracy refers to the ratio of correctly predicted samples to the total number of samples. *Precision* quantifies the proportion of samples classified as positive that are truly positive. *Recall* measures the proportion of actual positives correctly identified by the model. The F1 Score is a metric that combines Precision and Recall by calculating their harmonic mean. True Positives (*TP*) refer to the number of samples the model correctly predicts as belonging to a specific land use category, False Positives (*FP*) indicate the number of samples from other categories that the model incorrectly predicts as this land use category, and False Negatives (*FN*) represent the number of samples from a specific land use category that the model incorrectly predicts as belonging to other categories.

3.2.4. Metrics for Assessing the Correlation Between Land Utilization and Carbon Storage

The correlation between changes in land use over time and variations in carbon stock is examined by utilizing metrics that capture the dynamics of land use. The indices

used are the Single Land Use Dynamic Degree (SLUDD) [53], Comprehensive Land Use Dynamic Degree (LC) [54], and Entropy Index of Land Use Mix (LUM) [55]. SLUDD aims to emphasize the rate of change specific to a single Land Use and Land Cover (LULC) category. LC is linked to the overall rate of change in land use and the transformation of a particular Land Use and Land Cover (LULC) category into different LULC categories. An entropy index of land use mix assesses the degree of even distribution or mixture of different Land Use and Land Cover (LULC) categories within a specific year, reflecting the diversity of land usage.

$$SLUDD = \frac{U_b - U_a}{U_a} \times \frac{1}{T} \times 100\% \quad (19)$$

$$LC = \left[\frac{\sum_{i=1}^n \Delta LU_{i-j}}{2 \sum_{i=1}^n LU_i} \right] \times \frac{1}{T} \times 100\% \quad (20)$$

$$UM = A / (LN(N)) \quad (21)$$

U_a is the area of a land use type at the beginning of the study, U_b is the area of the land use type at the end of the study, T is the length of the study. LU_i is the area of a land use type of category i at the starting time of the study, ΔLU_{i-j} is the absolute value of the area of land of category i transformed into land use type of category j at the time of the study, and T is the length of the study. $A = (b_1/a) \ln(b_1/a) + (b_2/a) \ln(b_2/a) + \dots + (b_n/a) \ln(b_n/a)$. a = Total area of all land use types. b_n = area under land use type ' n '. N = Total number of land use types.

3.2.5. Spatial Dependence Between Land Use Dynamics and Carbon Stocks

The SLUDD, LC, and LUM indices were utilized as independent factors, while carbon stock was considered the dependent variable. These variables were used to assess the spatial relationship between land use and carbon stock using the spatial lag model (SLM) [56] and spatial error model (SEM) [56]. The fundamentals of SLM and SEM are as follows:

$$y_{SLM} = pW_y + X\beta + \varepsilon \quad (22)$$

y is the dependent variable, X is the explanatory variable matrix without an intercept term, W_y is the spatial weight matrix, β is the vector of slope indicating the influence of the independent variables over the dependent factor, ε is the vector of the random error terms.

$$y_{SEM} = X\beta + \lambda W_\varepsilon + \mu \quad (23)$$

λ is the spatial autoregressive coefficient following error term, μ is the Vectors of the error term, W_ε is the Spatial weight matrix.

3.3. Data Sources

This research utilized the first Landsat-derived 30 m annual Chinese Land Cover Dataset (CLCD) spanning the years 1999–2019 [50]. The classification includes nine distinct categories: cropland, forest, shrubland, grassland, water, snow and ice, barren land, impermeable surface, and wetland. Based on the current conditions of the research region and the land use categorization in this dataset, the land use/cover types were divided into seven distinct categories: cropland, forest, shrubland, grassland, water, barren land, and impervious surface. The determinants of Land Use and Land Cover (LULC) changes are crucial data inputs for conducting land use simulations. The driving factors of LULC changes are primarily derived from two socio-economic data points, one environmental data point, and three accessibility data points, as shown in Figure 5. Detailed data descriptions and sources are provided in Table 2. In this work, these determinants primarily consist of physico-geographical characteristics, accessibility, and socio-economic aspects.

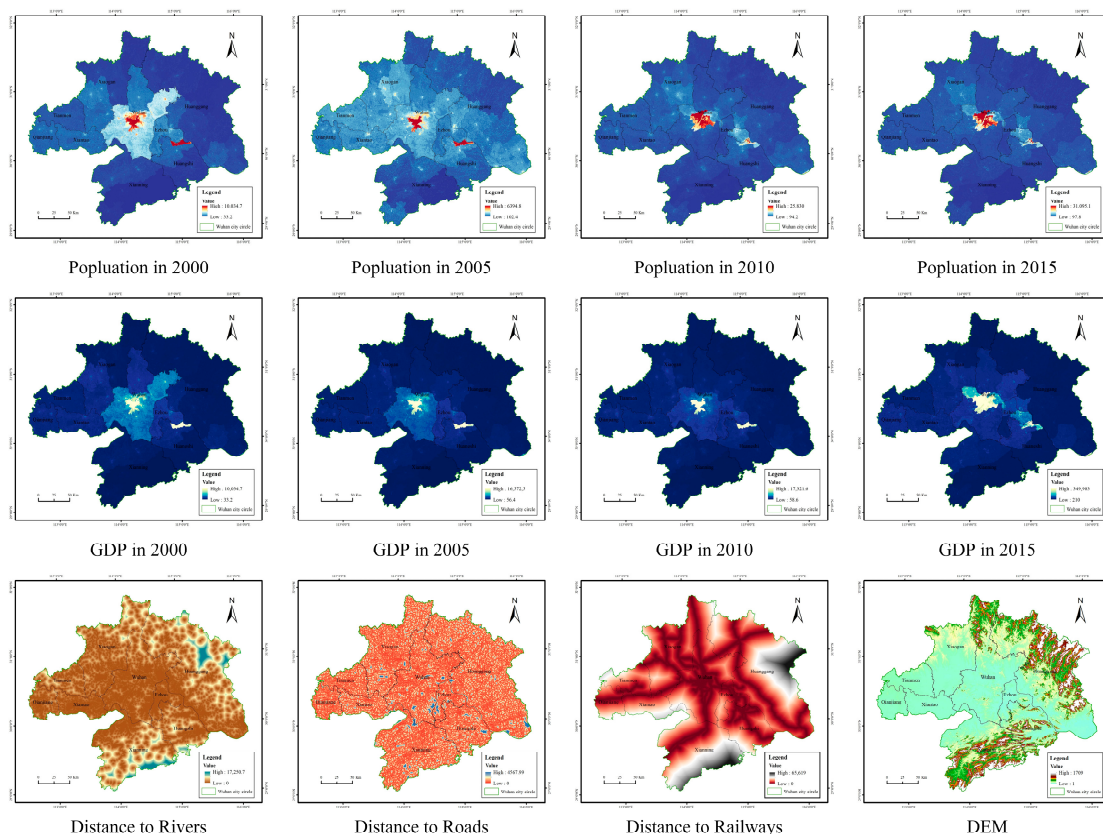


Figure 5. Auxiliary channel factorization diagram.

Table 2. Specific description of each driver and its source.

Specific Data	Resolution	Type	Source
Population	1000 m	Raster	Resource and Environment Science and Data Centre of the Chinese Academy of Sciences (https://www.resdc.cn/ , accessed on 25 April 2023)
GDP	1000 m	Raster	
DEM	30 m	Raster	NASA(National Aeronautics and Space Administration) and NGA (National Geospatial-Intelligence Agency) (https://www2.jpl.nasa.gov/srtm/ , accessed on 9 September 2023)
The distance to Rivers	30 m	Raster	National Catalogue Service for Geographic Information (https://www.webmap.cn/commres.do?method=result100 , accessed on 5 September 2023)
The distance to Railways	30 m	Raster	
The distance to Road	30 m	Raster	The distance module in ArcGIS 10.8 was used to calculate the distances from the shapefile format of each source data

4. Results

4.1. Analysis of LULC Prediction Results

Table 3 shows the combined performance scores of OS-CA (Open Space Cellular Automata Model) [57], ConvLSTM, and SA-ConvLSTM. From Table 3, it can be seen that both the ConvLSTM model and SA-ConvLSTM model based on the deep learning method perform better than the OS-CA model.

Table 3. Comparison of the prediction results of the three models. The best results are marked in bold.

Model	Accuracy	Precision	Recall	F1	Kappa
OS-CA	94.629%	81.879%	78.321%	80.061%	90.498%
ConvLSTM	99.313%	95.173%	95.460%	95.277%	98.820%
SA-ConvLSTM	99.325%	95.337%	96.549%	95.919%	98.884%

The extrapolation performance of the SA-ConvLSTM model is superior to that of the ConvLSTM model. Among the seven land use classifications, shrubland, grassland, and barren land accounted for only 0.003%, 0.037%, and 0.008% of the total land area, respectively. However, due to the uneven distribution of data samples, further analysis is needed to better understand the accuracy of the predictions. To address the uneven distribution of data samples, it is necessary to gain a more comprehensive understanding of the prediction performance. Table 4 compares the prediction accuracy for small data samples, with the best results highlighted in bold.

Table 4. Accuracy of the three models for each category. The best results are marked in bold.

Evaluation Indicators	Type		Cropland	Forest	Shrubs	Grassland	Water	Barren	Impervious
	Model								
Accuracy	OS-CA		91.42%	91.00%	70.37%	35.85%	79.34%	36.98%	81.36%
	ConvLSTM		98.78%	99.06%	85.63%	78.27%	96.16%	78.91%	98.15%
	SA-ConvLSTM		98.79%	99.05%	87.52%	78.96%	96.20%	88.35%	98.14%
Precision	OS-CA		95.52%	95.29%	86.33%	64.62%	91.82%	53.99%	85.58%
	ConvLSTM		99.57%	99.41%	89.84%	85.75%	96.72%	94.49%	99.90%
	SA-ConvLSTM		99.58%	99.41%	90.64%	86.09%	96.74%	95.02%	99.91%
Recall	OS-CA		95.52%	95.29%	79.19%	44.60%	85.38%	53.99%	94.28%
	ConvLSTM		99.20%	99.64%	94.81%	89.97%	99.39%	82.71%	98.21%
	SA-ConvLSTM		99.21%	99.64%	96.22%	90.51%	99.42%	92.63%	98.23%
F1	OS-CA		95.52%	95.29%	82.61%	52.77%	88.48%	53.99%	89.72%
	ConvLSTM		99.39%	99.52%	92.26%	87.81%	98.03%	88.21%	99.05%
	SA-ConvLSTM		99.39%	99.53%	93.34%	88.24%	98.06%	93.81%	99.06%

Table 4 demonstrates that both ConvLSTM and SA-ConvLSTM models can predict land use patterns after training, and the Self-Attention Memory Module (SAM) enhances the prediction accuracy for small-sample categories. The feasibility of the SA-ConvLSTM model in predicting time-series land use data is demonstrated, offering a new approach for analyzing land use development patterns through deep learning.

The SAM module helps the SA-ConvLSTM network capture long-range connections and contextual information in input data, adding value. This is performed by allowing the network to focus on input sequence parts or attributes that are most important to each time step prediction. This concentrating mechanism allows the network to dynamically assign different degrees of relevance to geographical and temporal characteristics, improving its ability to capture complex data patterns and linkages. In occupations where long-distance interactions or dependencies are vital for exact prediction, it may capture long-term dependencies.

The data in Figure 6 demonstrate that both the ConvLSTM and SA-ConvLSTM models accurately predict changes over a 5-year period, in contrast to the OS-CA model, whose accuracy decreases with time. However, due to the limited area of shrubland, grassland, and barren land categories in the land use dataset (CLCD), areas with significant and obvious changes could not be accurately identified, limiting the demonstration of the advantages of SA-ConvLSTM over ConvLSTM. Therefore, we selected Guanggu, a regional center within the Wuhan City Circle. Both the ConvLSTM and SA-ConvLSTM models accurately represent the city's dynamic characteristics in terms of cropland, forest land, water bodies, and impervious surfaces during the urban development period from 2009 to 2018.

The SA-ConvLSTM model has a powerful feature learning capability and can effectively integrate multiple data sources. Incorporating population and GDP data can enhance the model's understanding of urban development changes. Additionally, the model incorporates geographic and economic evaluation factors to enhance its understanding of similar or non-similar land use change [58]. Distances to roads, rivers, and railroads can help understand the variability of land changes caused by human engineering activities in the study area [59]. In addition, DEMs can introduce dynamic facilitating or limiting factors [60]. The ConvLSTM module captures localized patterns, while the self-attention

module provides a broader context to further improve the model's understanding of land use change [61]. Furthermore, the SA-ConvLSTM model demonstrates superior capability in simulating urban sprawl dynamics compared to traditional land use change modeling techniques. This study aims to achieve the integrated use of multiple data sources. Due to its powerful feature extraction capabilities, deep learning shows great potential as a tool for predicting land use in time-series data.

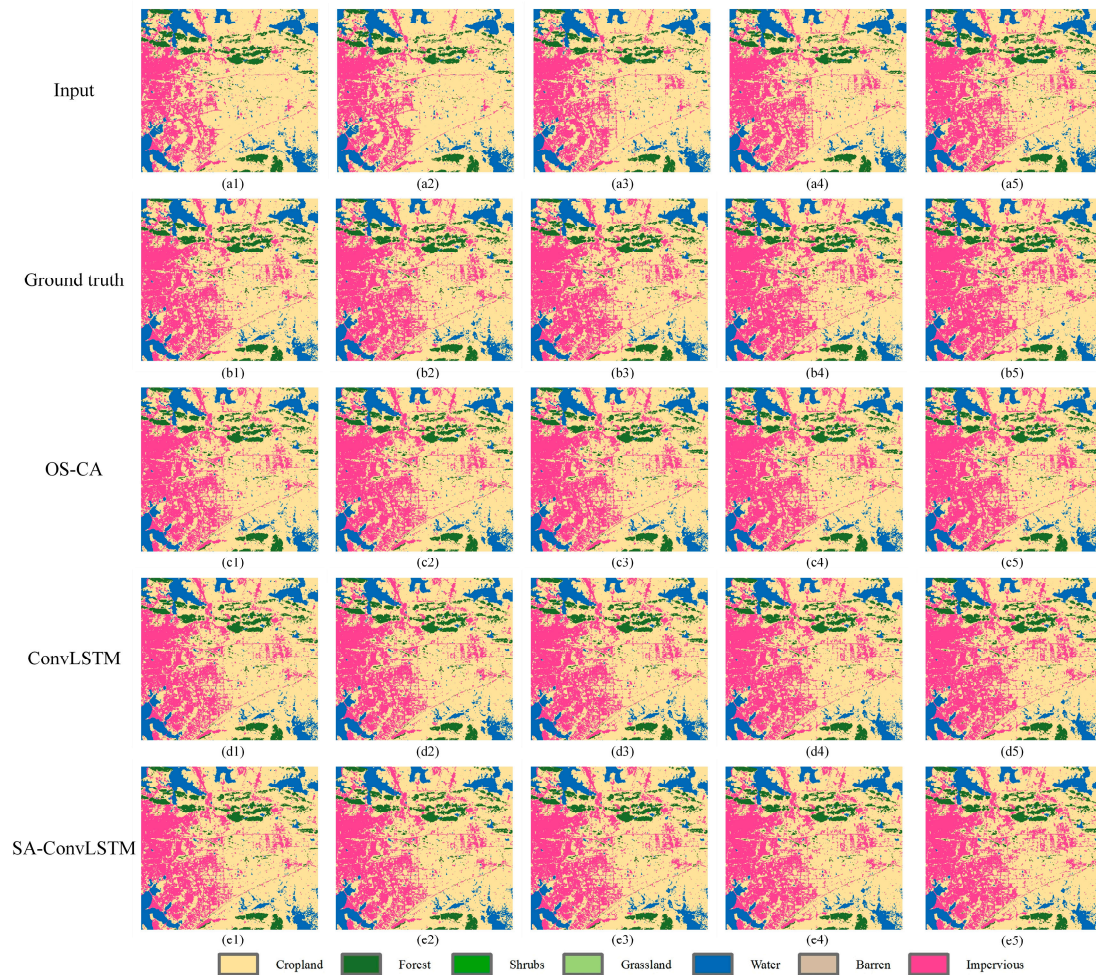


Figure 6. Visualization results for the regional center Guanggu: (a1–a5) indicate some of the inputs to the model; (b1–b5) ground-truth land use maps for the years 2014, 2015, 2016, 2017, and 2018; (c1–c5), (d1–d5) and (e1–e5) are the corresponding predictions of OS-CA, ConvLSTM and SA-ConvLSTM, respectively.

4.2. Carbon Stock Dynamics in Wuhan City Circle from 1999 to 2018

The carbon module of the InVEST model indicates that the carbon stock in the Wuhan urban area was 6.75×10^8 MgC in 1999 and decreased to 6.68×10^8 MgC in 2018. From 1999 to 2018, the carbon stock in the urban area experienced a notable decline, with a total reduction of 6.49×10^6 MgC. The carbon stock of different land use categories, listed in decreasing order, is as follows: cropland, forest, water bodies, impervious, grassland, shrubs, and barren land.

Figure 7 shows that the geographic distribution of carbon storage in the Wuhan metropolitan area from 1999 to 2018 exhibited no significant variation. Most areas within the metropolitan region experienced minimal changes in carbon storage. Reductions in carbon storage primarily occurred in areas undergoing urbanization, while increases were concentrated in regions with newly established forests and farmland. Over the period from 1999 to 2018, carbon storage remained generally stable across most regions. For the Wuhan urban circle, the areas of carbon stock reduction are primarily forests and water

bodies, while the sources of increased carbon stock are mainly the conversion of forests and grasslands to land types with higher carbon densities. However, the conversion of agricultural land near the urban center led to a decline in carbon storage. The carbon storage within national nature reserves in the Wuhan metropolitan area remained stable due to the implementation of ecological conservation measures, highlighting the effectiveness of these policies in protecting carbon storage.

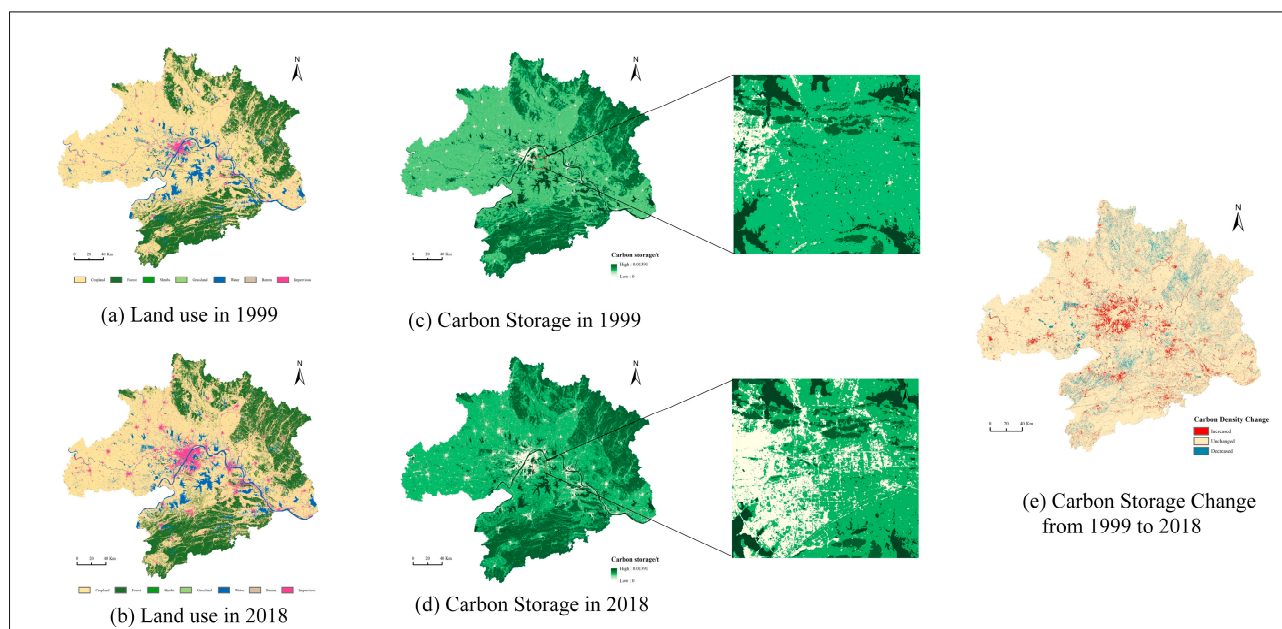


Figure 7. (a) Land use in 1999; (b) Land use in 2018; (c) Spatial distribution of carbon stocks in 1999; (d) Spatial distribution of carbon stocks in 2018; (e) Map of carbon stock changes in the study area from 1999 to 2018.

Table S1 indicates that above-ground carbon storage in Wuhan's urban area increased by 204,403 MgC, while below-ground carbon storage decreased by 2,292,636.9 MgC, soil carbon storage declined by 4,174,011.8 MgC, and dead organic matter carbon storage reduced by 224,241.6 MgC, resulting in a total decrease of 6,486,487.3 MgC. The estimated results are subject to an error margin of $\pm 25\%$, owing to model uncertainties [62] and the precision of land use data [50]. In terms of land use changes, the primary drivers of carbon storage reduction from 1999 to 2018 included the conversion of cropland to impervious surfaces, forests to cropland and impervious surfaces, and water bodies to cropland and impervious surfaces. The main sources of carbon storage increase were the conversion of cropland to forests and water bodies. With the development of the metropolitan area, farmlands have likely been subdivided into smaller plots. The urban area of Wuhan, characterized by economic prosperity, high urbanization rates, dense population, and rugged terrain, has experienced extensive land development. This urban expansion has encroached upon large agricultural, forested, and water bodies, making it a primary driver of carbon storage reduction within the Wuhan metropolitan area. Urbanization activities, such as road and building construction, lead to soil compaction and degradation, thereby weakening the carbon retention capacity of farmland.

4.3. Prediction of Carbon Storage in the Wuhan City Circle in 2023

The carbon module of the InVEST model indicates that the carbon stock in the Wuhan urban area was 6.69×10^8 MgC in 2018, increasing to 6.69×10^8 MgC in 2023. From 2018 to 2023, the carbon stock in the urban area had a significant rise, increasing by a total of 9.17×10^4 MgC. Carbon stocks in different land use categories are in the following order: cropland, forest, water bodies, impervious, grassland, shrubs, and barren land.

Figure 8 indicates that the geographic distribution of carbon storage in the Wuhan metropolitan area from 2018 to 2023 showed no significant variation. Most areas within the metropolitan region experienced minimal changes in carbon storage. Increases in carbon storage mainly occurred in areas undergoing urbanization, while significant growth was observed in regions with newly established forests and water bodies. Throughout this period, carbon storage remained generally stable across most regions.

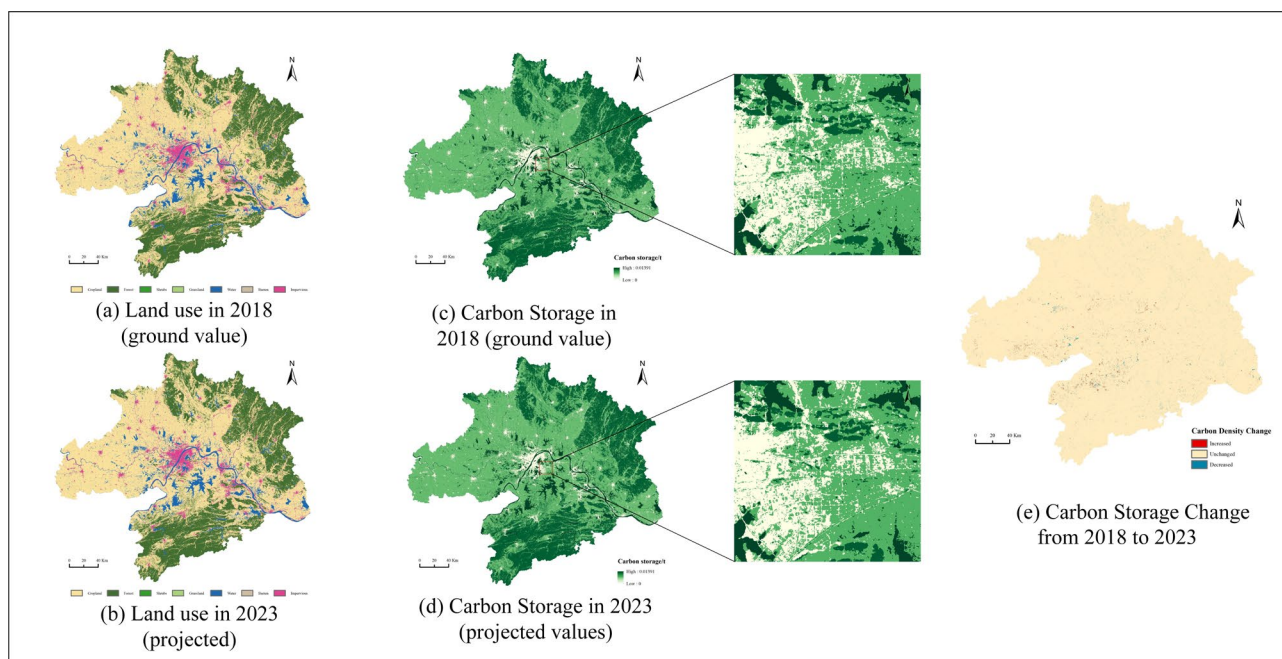


Figure 8. (a) Land use in 2018; (b) Land use in 2023; (c) Spatial distribution of carbon stocks in 2018; (d) Spatial distribution of carbon stocks in 2023; (e) Map of carbon stock changes in the study area from 2018 to 2023.

Table S2 shows that from 2018 to 2023, above-ground carbon storage in Wuhan's urban area increased by 158,093.1 MgC, while below-ground carbon storage decreased by 99,746.8 MgC, soil carbon storage rose by 147,011 MgC, and dead organic matter carbon storage decreased by 113,645.1 MgC, leading to a net increase of 91,712.1 MgC in total carbon storage. The estimated results are subject to an error margin of $\pm 25\%$, owing to model uncertainties and the precision of land use data. Areas with increased carbon storage were primarily forests and water bodies, with the main drivers of this increase being the conversion of cropland to forests and water bodies. In contrast, reductions in carbon storage were mainly due to the conversion of water bodies to cropland, forests to cropland, and cropland to impervious surfaces. These findings underscore the critical role of afforestation and the conversion of cropland to water bodies in enhancing carbon storage, highlighting the importance of forests and water bodies in the ecosystem's carbon storage function. The results also reveal that impervious urban surfaces have gradually transformed into water bodies and barren land, while barren land has shifted to cropland, forests, grasslands, and water bodies. Additionally, shrubs have been converted into cropland, forests, and grasslands, reflecting the positive impact of ecological protection policies on carbon storage amid rapid urbanization. A degree of cropland preservation, along with policies encouraging afforestation and conversion to water bodies, can effectively mitigate carbon storage loss. Understanding the relationship between land use and carbon storage is essential for effective land use planning and carbon management strategies. Policymakers and urban planners should consider the carbon impact of land use decisions to support sustainable development.

4.4. Effects of Land Use/Land Cover Change on Carbon Stock

This study demonstrates how carbon stock pools are impacted by LULC changes from 1999 to 2023. According to the InVEST carbon model, within the Wuhan urban circle, carbon stocks in croplands are higher than those in forests, impervious surfaces, and grasslands. As shown in Figure 9, during the 25-year period, carbon stocks in soil and forests generally declined, followed by a sharp increase between 2008 and 2013. This increase may be attributed to significant infrastructure developments initiated in the Wuhan urban area around 2008. Subsequently, the expansion of urban areas resulted in reduced cropland and forest areas. Post-2018, changes in cropland and forest areas were mitigated by stringent cropland protection measures and policies advocating the reforestation of agricultural land. The expansion of urban infrastructure in the Wuhan urban area from 2008 to 2018 occurred at the expense of land use types such as cropland, forest, and grassland. Under the direction of policy-driven sustainable development, the extent of land use change is increasingly limited, while carbon stock itself requires a long period to undergo significant changes. As a result, the impact of land use transitions on carbon stock is less likely to exhibit noticeable trends within a 5-year period.

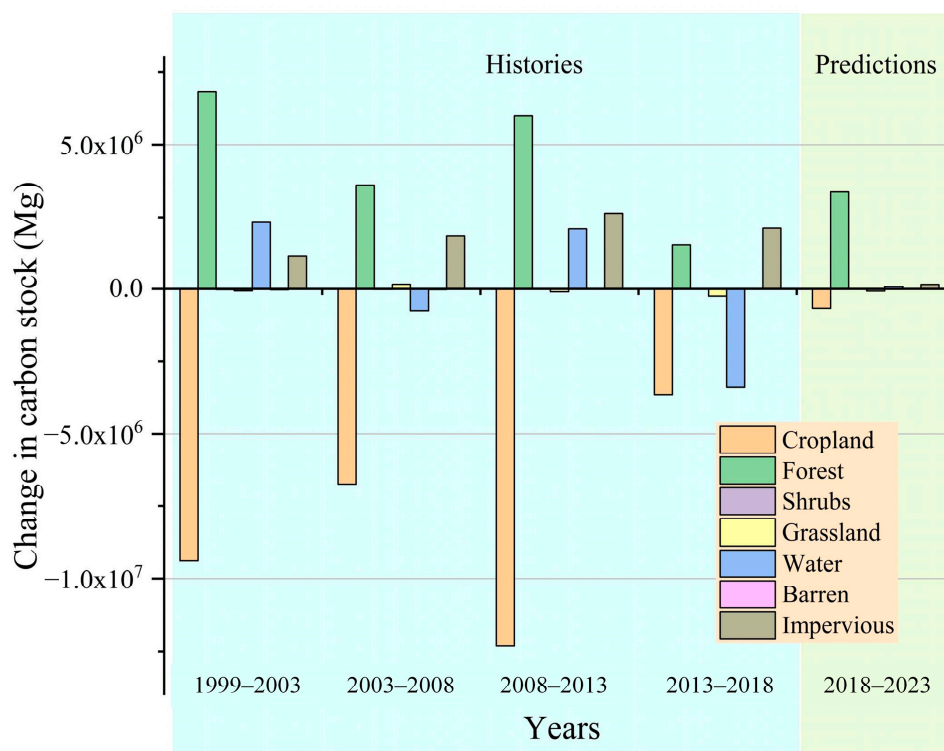


Figure 9. Carbon stocks from 1999 to 2023.

4.5. Changes in the Land Use Dynamics from 1999 to 2023

From 1999 to 2018, the dynamics of LULC are presented in the form of annual rates of change in SLUDD, LC, and LUM. The first two indices closely correlate with the inter-annual change rate in the LULC category, while the third index concentrates on the variability of land use patterns. Figure 10 presents the output associated with these indices. Tables S3 and S4 in the Supplementary Information offer detailed tabular data for each region regarding the different indicators mentioned above.

other districts experienced a decrease in the net area of agricultural land. District 10 experienced the highest increase in the SLUDD area of forests, with an annual growth rate of 42.4%. The closer the forest area is to the center of the Wuhan urban area, the more significant the decrease, as observed in Districts 38, 44, and 36, among others. No increases in the SLUDD of shrubs are observed across the districts, and nearly half of these districts exhibit no changes in the SLUDD of shrubs. This lack of change is attributable to the shrub category's very small proportion in the Wuhan urban area. The Wuhan City Circle shows a notable absence of a shrub category, with districts 17, 4, and 5, among others, undergoing a decline. The districts with the highest increases in the SLUDD of grassland—17, 18, and 22—are located primarily in the central and southern parts of the Wuhan City Circle, likely due to the eco-watershed management of the region. The five districts experiencing a five percent decrease include districts 38, 46, 40, 14, and 13, all located in the old urban area. This decrease is likely due to the reduction in grassland areas resulting from improved infrastructure. Additionally, the diminished SLUDD area of water bodies is primarily found in the central urban areas, likely resulting from increased land and road resource demands driven by population growth, leading to partial lake infillings. District 16 experienced the largest increase in water body area, at 3.52%, followed by District 31 with 1.14%. Districts 1 and 2 are the only areas with positive growth in the SLUDD of barren lands, recording annual growth rates of 820% and 245%, respectively. Simultaneously, these districts have seen significant increases in impervious surfaces, likely due to the geographic characteristics of Districts 1 and 2 over the past two decades. Initially, land was converted from agricultural, forestry, and water uses to barren land and subsequently prepped for development into impervious surfaces. All areas designated as impervious surfaces experienced positive growth, particularly in the new urban centers of the Wuhan City Circle—notably, districts 1, 2, 3, and 4. These districts likely represent areas where urban expansion offers lower costs and higher benefits. However, the old urban areas in the central region of the Wuhan City Circle and the outer ring exhibit lower growth rates, specifically in districts 37, 40, and 45. This slowdown is likely due to the higher renovation costs in the old urban areas and the diminished benefits of expanding more distant urban areas. Table S4 from the Supplementary Materials indicates that from 2018 to 2023, cropland SLUDD shifted from only two areas showing growth to twelve; forest SLUDD continued to decline, more so nearer the center; shrub SLUDD saw growth in six areas, up from none; grassland SLUDD showed no growth; water body SLUDD increased most significantly in Area 1 and least in District 33; barren land SLUDD showed no growth; impervious surface SLUDD changes were more dispersed, with central districts like 37 and 40 unchanged, while Districts 38, 36, and 42 experienced slight increases.

LC is designed to reveal the annual rate of conversion from one LULC type to another across the total area, illustrating the overall rate of land use change throughout the region. Table S3 reveals that the regions with the largest increases from 1999 to 2018 were all key areas within the Wuhan City Circle. Table S4 shows that between 2018 and 2023, the regions experiencing the largest growth rates were primarily the 43rd, 1st, and 39th districts, with the remaining top ten comprising neighboring cities.

LUM measures the degree of uniform distribution and integration of land use within a specific area. Its primary advantage is that it promotes the diversity and balance of land use types in that area. Table S3 indicates that from 1999 to 2018, the areas with the most significant changes in LUM were economically prosperous urban areas, notably districts 36, 37, and 38. Table S4 reveals that from 2018 to 2023, the districts with the most changes in LUM were the 18th, 33rd, and 43rd. These districts, while having fewer lakes compared to others, feature a more developed urban base, potentially enhancing land use diversity.

4.6. Spatial Dependence Between Changes in Land Use Dynamics and Carbon Stocks

This study employed the spatial lag model and the spatial error model to examine the spatial dependence of interannual Land Use and Land Cover dynamics across two periods: 1999 to 2018 and 2018 to 2023. Tables 5 and 6 showcase the principal findings

from the spatial lag regression analysis and the spatial error model analysis. The Breusch–Pagan test applied to the spatial lag model and the likelihood ratio test assessing spatial error dependence within the spatial error model both yielded results that are statistically significant, with significance levels below 0.05.

Table 5. Results of spatial error and spatial lag regression models for various LULC types from 1999 to 2018.

Output of Spatial Lag Regression (1999–2018)					Output of Spatial Error Model (1999–2018)				
Variable	Coefficient	Std. Error	z-Value	Probability	Variable	Coefficient	Std. Error	z-Value	Probability
CONSTANT	137.05	111.79	1.23	0.22	CONSTANT	216.84	149.62	1.45	0.15
SLUDD_CL	−54.55	104.68	−0.52	0.60	SLUDD_CL	−47.19	101.30	−0.47	0.64
SLUDD_FL	−1.18	5.96	−0.20	0.84	SLUDD_FL	−1.58	4.92	−0.32	0.75
SLUDD_SL	1.71	20.94	0.08	0.94	SLUDD_SL	24.56	22.08	1.11	0.27
SLUDD_GL	0.42	1.76	0.24	0.81	SLUDD_GL	−0.90	1.69	−0.53	0.60
SLUDD_WL	−74.47	47.12	−1.58	0.11	SLUDD_WL	−119.53	45.14	−2.65	0.008 **
SLUDD_BL	−0.52	0.31	−1.68	0.09	SLUDD_BL	−0.45	0.26	−1.74	0.08
SLUDD_IL	−25.81	15.01	−1.72	0.09	SLUDD_IL	−33.17	15.59	−2.13	0.033 *
LC	−184.78	201.29	−0.92	0.36	LC	−208.37	165.71	−1.26	0.21
Changes in LUM(%)	−486.53	1189.57	−0.41	0.68	Changes in LUM(%)	−410.90	1271.31	−0.32	0.75
W_CC_SUM	0.56	0.13	4.36	0.000 **	LAMBDA	0.74	0.09	7.92	0.000 **

* $p < 0.05$, ** $p < 0.01$.

Table 6. Results of spatial error and spatial lag regression models for various LULC types from 2018 to 2023.

Output of Spatial Lag Regression (2019–2023)					Output of Spatial Error Model (2019–2023)				
Variable	Coefficient	Std. Error	z-Value	Probability	Variable	Coefficient	Std. Error	z-Value	Probability
CONSTANT	1.30	10.03	0.13	0.90	CONSTANT	1.93	9.34	0.21	0.84
SLUDD_CL	−173.57	94.03	−1.85	0.07	SLUDD_CL	−132.82	86.26	−1.54	0.12
SLUDD_FL	43.88	21.20	2.07	0.038 *	SLUDD_FL	55.68	21.01	2.65	0.008 **
SLUDD_SL	8.03	12.05	0.67	0.51	SLUDD_SL	0.03	11.52	0.00	1.00
SLUDD_GL	5.94	2.30	2.59	0.010 **	SLUDD_GL	7.73	2.14	3.62	0.000 **
SLUDD_WL	−302.68	33.78	−8.96	0.000 **	SLUDD_WL	−305.17	31.07	−9.82	0.000 **
SLUDD_BL	−1.78	1.76	−1.01	0.31	SLUDD_BL	−0.83	1.73	−0.48	0.63
SLUDD_IL	−97.61	139.17	−0.70	0.48	SLUDD_IL	−30.11	138.35	−0.22	0.83
LC	475.95	305.84	1.56	0.12	LC	627.53	295.85	2.12	0.034 *
Changes in LUM(%)	1197.77	1682.75	0.71	0.48	Changes in LUM(%)	920.24	1588.93	0.58	0.56
W_CC_SUM	−0.17	0.12	−1.50	0.13	LAMBDA	−0.45	0.20	−2.29	0.022*

* $p < 0.05$, ** $p < 0.01$.

Table 6 demonstrates that from 1999 to 2018, the seven impact factor variables of SLUDD, LC, and LUM associated with cropland, forest, shrubland, grassland, and barren land were not statistically significant ($p > 0.05$). The regression coefficient for the SLUDD of water is -119.532 , indicating a significant negative impact on carbon stocks at the 0.01 level of significance ($p = 0.008 < 0.01$). The regression coefficient for the SLUDD of previous years is -33.165 , which demonstrates a significant negative impact on carbon stocks at the 0.05 significance level ($p = 0.033 < 0.05$). The regression coefficient for the residual spatial lag variable LAMBDA is 0.741 , indicating a significant positive impact on carbon stocks at a 0.01 level of significance ($p = 0.000 < 0.01$).

Table 6 reveals that the four impact factor variables of the SLUDD and LUM associated with cropland, shrubs, barren lands, and impervious surfaces were not statistically significant ($p > 0.05$) from 2018 to 2023. The regression coefficient for the SLUDD of forest is 55.677 , indicating a significant positive impact on carbon stocks at the 0.01 significance level ($p = 0.008 < 0.01$). The regression coefficient for the SLUDD of grassland is 7.733 , indicating a significant positive effect on carbon stocks at a 0.01 significance level ($p = 0.000 < 0.01$). The regression coefficient for the SLUDD of water is -305.170 , demonstrating a significant negative effect on carbon stocks at the 0.01 significance level ($p = 0.000 < 0.01$). The regres-

sion coefficient for LC is 627.532, indicating a significant positive effect on carbon stocks at the 0.05 significance level ($p = 0.034 < 0.05$). The regression coefficient for the residual spatial lag variable LAMBDA is -0.451 , indicating a significant negative impact on carbon stocks at the 0.05 significance level ($p = 0.022 < 0.05$).

5. Discussion

This paper presents the SA-ConvLSTM model, a hybrid approach that integrates the InVEST model for forecasting carbon stock. The SA-ConvLSTM model extends the original ConvLSTM by incorporating the self-attention mechanism. To improve the accuracy of land use predictions, additional auxiliary factors are integrated with time-series land use data. Moreover, multiple data sources are utilized in the prediction process. The ConvLSTM model effectively captures both spatial and temporal information from time-series land use data. The self-attention memory module significantly enhances the model's ability to process global contextual information. Geographic and economic auxiliary factor data help guide and reinforce developmental changes. The encoder–decoder structure is employed to enhance the smoothness of the model training process. The experimental findings demonstrate that the model effectively captures the characteristics of land use alterations and produces predictions that are more accurate than those of the ConvLSTM model.

Our research findings indicate that the carbon stock of the Wuhan urban circle in 1999, 2008, and 2018 were 6.72×10^8 MgC, 6.71×10^8 MgC, and 6.65×10^8 MgC, respectively. The primary drivers of these changes include rapid population growth and development policies focused on urban expansion, which accelerated the conversion of cropland and forests, thereby impacting the region's carbon stocks. Additionally, insufficient monitoring and planning of natural resources have emerged as critical factors influencing the balance between natural and urban ecosystems.

Previous literature has indicated that urban expansion results in carbon stock losses associated with the loss of agricultural land and forests [63], a finding that is also observed in this study. Furthermore, as forests and agricultural land serve as species-rich habitats and provide valuable ecosystem services, the loss of forests and wetlands due to urban expansion is evident not only in Wuhan but also globally [64]. Compared to the results of J Zhang [32], the carbon stock calculated in this study is higher. The discrepancy can be attributed to the following reason: J Zhang's study did not distinguish between different water bodies, and the carbon stocks of the turbulent Yangtze River and lake wetlands were both uniformly calculated as water bodies, which warrants further investigation.

This research is limited by the need for more precise land use data for SA-ConvLSTM and by the temporal variability of carbon density, influenced by factors such as precipitation, temperature, and soil organic carbon sensitivity. Additionally, regularly updated carbon pool densities are necessary. Expanding this study's scope to examine land use changes across various urban areas and conducting a more comprehensive analysis of the underlying factors and external impacts on urban growth could broaden its findings.

6. Conclusions

This paper proposes a spatio-temporal land use prediction model utilizing SA-ConvLSTM. By integrating the SA-ConvLSTM model with the InVEST, SLM, and SEM models, a comprehensive prediction and evaluation system of carbon stock is established to assess the impact of land use changes on carbon stock in the Wuhan City Circle. The following conclusions are drawn:

1. Compared to the traditional metacellular automata prediction method, the SA-ConvLSTM model demonstrates a 4.7% improvement in prediction accuracy. Furthermore, compared to traditional ConvLSTM, the self-attention memory module enhances the model's prediction accuracy for small sample sizes.
2. From 1999 to 2018, the carbon stock in the Wuhan City Circle exhibited a decreasing trend, with an overall decline of 6.49×10^6 MgC. The primary cause of this reduction is the encroachment of arable land due to rapid urbanization. From 2018 to 2023,

the predicted carbon stock in the Wuhan urban circle was expected to increase by 9.17×10^4 MgC, primarily due to the conversion of water bodies into cropland, followed by the reforestation of cropland.

3. The historical spatial error model suggests that a decrease of 1 unit in carbon stock change corresponds to an increase of 119 units in the SLUDD of water bodies and 33 units in impervious surfaces. The future spatial error model suggests that for each unit increase in carbon stock changes, the SLUDD would increase by 55 units for forests, 7 units for grasslands, and decrease by 305 units for water bodies.

Supplementary Materials: The following supporting information can be downloaded at: <https://www.mdpi.com/article/10.3390/rs16234372/s1>, Table S1. Changes in carbon storage caused by land use change, 1999–2018; Table S2. Changes in carbon storage caused by land use change, 2018–2023; Table S3: Changes in LC, changes in LUM, and annual changes in SLUDD for each LULC type in Wuhan from 1999 to 2018; Table S4: Changes in LC, changes in LUM, and annual changes in SLUDD for each LULC type in Wuhan from 2018 to 2023.

Author Contributions: Z.Z.: writing—original draft, data curation, formal analysis, investigation, methodology, software, conceptualization, and visualization. X.W.: writing—original draft, investigation, methodology, conceptualization, and funding acquisition. B.P.: writing—review and editing. All authors have read and agreed to the published version of the manuscript.

Funding: This work is jointly supported by the National Natural Science Foundation of China [grant number 42071429] and the Open Fund of Key Laboratory of Urban Land Resources Monitoring and Simulation, Ministry of Natural Resources [grant number KF-2023-08-19].

Data Availability Statement: The data supporting the findings of this study are available from the corresponding author upon reasonable request.

Conflicts of Interest: The authors declare no conflicts of interest.

References

1. Houghton, R.A. Land-use change and the carbon cycle. *Glob. Chang. Biol.* **1995**, *1*, 275–287. [[CrossRef](#)]
2. Mitra, S.; Wassmann, R.; Vlek, P.L. An appraisal of global wetland area and its organic carbon stock. *Curr. Sci.* **2005**, *88*, 25–35.
3. Shin, Y.J.; Midgley, G.F.; Archer, E.R.; Arneeth, A.; Barnes, D.K.; Chan, L.; Hashimoto, S.; Hoegh-Guldberg, O.; Inzarov, G.; Leadley, P. Actions to halt biodiversity loss generally benefit the climate. *Glob. Chang. Biol.* **2022**, *28*, 2846–2874. [[CrossRef](#)] [[PubMed](#)]
4. Walker, W.S.; Gorelik, S.R.; Cook-Patton, S.C.; Baccini, A.; Farina, M.K.; Solvik, K.K.; Ellis, P.W.; Sanderman, J.; Houghton, R.A.; Leavitt, S.M. The global potential for increased storage of carbon on land. *Proc. Natl. Acad. Sci. USA* **2022**, *119*, e2111312119. [[CrossRef](#)] [[PubMed](#)]
5. Fawzy, S.; Osman, A.I.; Doran, J.; Rooney, D.W. Strategies for mitigation of climate change: A review. *Environ. Chem. Lett.* **2020**, *18*, 2069–2094. [[CrossRef](#)]
6. Pendleton, L.; Donato, D.C.; Murray, B.C.; Crooks, S.; Jenkins, W.A.; Sifleet, S.; Craft, C.; Fourqurean, J.W.; Kauffman, J.B.; Marbà, N. Estimating global “blue carbon” emissions from conversion and degradation of vegetated coastal ecosystems. *PLoS ONE* **2012**, *7*, e43542. [[CrossRef](#)]
7. Georgiou, K.; Jackson, R.B.; Vindušková, O.; Abramoff, R.Z.; Ahlström, A.; Feng, W.; Harden, J.W.; Pellegrini, A.F.; Polley, H.W.; Soong, J.L. Global stocks and capacity of mineral-associated soil organic carbon. *Nat. Commun.* **2022**, *13*, 3797. [[CrossRef](#)]
8. Wiesmeier, M.; Urbanski, L.; Hobbey, E.; Lang, B.; von Lützow, M.; Marin-Spiotta, E.; van Wesemael, B.; Rabot, E.; Ließ, M.; Garcia-Franco, N. Soil organic carbon storage as a key function of soils—A review of drivers and indicators at various scales. *Geoderma* **2019**, *333*, 149–162. [[CrossRef](#)]
9. Ledo, A.; Smith, P.; Zerihun, A.; Whitaker, J.; Vicente-Vicente, J.L.; Qin, Z.; McNamara, N.P.; Zinn, Y.L.; Llorente, M.; Liebig, M. Changes in soil organic carbon under perennial crops. *Glob. Chang. Biol.* **2020**, *26*, 4158–4168. [[CrossRef](#)]
10. Luo, Z.; Viscarra Rossel, R.A.; Shi, Z. Distinct controls over the temporal dynamics of soil carbon fractions after land use change. *Glob. Chang. Biol.* **2020**, *26*, 4614–4625. [[CrossRef](#)]
11. Goetz, S.J.; Baccini, A.; Laporte, N.T.; Johns, T.; Walker, W.; Kellndorfer, J.; Houghton, R.A.; Sun, M. Mapping and monitoring carbon stocks with satellite observations: A comparison of methods. *Carbon Balance Manag.* **2009**, *4*, 2. [[CrossRef](#)] [[PubMed](#)]
12. Smith, P. How to measure, report and verify soil carbon change. In Proceedings of the AGU Fall Meeting Abstracts, New Orleans, LA, USA, 13–17 December 2021; p. GC41D–01.
13. Angelopoulou, T.; Balafoutis, A.; Zalidis, G.; Bochtis, D. From laboratory to proximal sensing spectroscopy for soil organic carbon estimation—A review. *Sustainability* **2020**, *12*, 443. [[CrossRef](#)]

14. Ciais, P.; Dolman, A.J.; Bombelli, A.; Duren, R.; Peregon, A.; Rayner, P.J.; Miller, C.; Gobron, N.; Kinderman, G.; Marland, G. Current systematic carbon-cycle observations and the need for implementing a policy-relevant carbon observing system. *Biogeosciences* **2014**, *11*, 3547–3602. [[CrossRef](#)]
15. Goetz, S.; Dubayah, R. Advances in remote sensing technology and implications for measuring and monitoring forest carbon stocks and change. *Carbon Manag.* **2011**, *2*, 231–244. [[CrossRef](#)]
16. Padarian, J.; Stockmann, U.; Minasny, B.; McBratney, A. Monitoring changes in global soil organic carbon stocks from space. *Remote Sens. Environ.* **2022**, *281*, 113260. [[CrossRef](#)]
17. Li, T.; Xia, A.; McLaren, T.I.; Pandey, R.; Xu, Z.; Liu, H.; Manning, S.; Madgett, O.; Duncan, S.; Rasmussen, P. Preliminary Results in Innovative Solutions for Soil Carbon Estimation: Integrating Remote Sensing, Machine Learning, and Proximal Sensing Spectroscopy. *Remote Sens.* **2023**, *15*, 5571. [[CrossRef](#)]
18. Zhang, M.; Du, H.; Mao, F.; Zhou, G.; Li, X.; Dong, L.; Zheng, J.; Zhu, D.e.; Liu, H.; Huang, Z. Spatiotemporal evolution of urban expansion using Landsat time series data and assessment of its influences on forests. *ISPRS Int. J. Geo-Inf.* **2020**, *9*, 64. [[CrossRef](#)]
19. Adhikari, K.; Owens, P.R.; Libohova, Z.; Miller, D.M.; Wills, S.A.; Nemecek, J. Assessing soil organic carbon stock of Wisconsin, USA and its fate under future land use and climate change. *Sci. Total Environ.* **2019**, *667*, 833–845. [[CrossRef](#)]
20. Li, Z.-L.; Tang, R.; Wan, Z.; Bi, Y.; Zhou, C.; Tang, B.; Yan, G.; Zhang, X. A review of current methodologies for regional evapotranspiration estimation from remotely sensed data. *Sensors* **2009**, *9*, 3801–3853. [[CrossRef](#)]
21. Leh, M.D.; Matlock, M.D.; Cummings, E.C.; Nalley, L.L. Quantifying and mapping multiple ecosystem services change in West Africa. *Agric. Ecosyst. Environ.* **2013**, *165*, 6–18. [[CrossRef](#)]
22. He, C.; Zhang, D.; Huang, Q.; Zhao, Y. Assessing the potential impacts of urban expansion on regional carbon storage by linking the LUSD-urban and InVEST models. *Environ. Model. Softw.* **2016**, *75*, 44–58. [[CrossRef](#)]
23. Babbar, D.; Areendran, G.; Sahana, M.; Sarma, K.; Raj, K.; Sivadas, A. Assessment and prediction of carbon sequestration using Markov chain and InVEST model in Sariska Tiger Reserve, India. *J. Clean. Prod.* **2021**, *278*, 123333. [[CrossRef](#)]
24. Wang, Z.; Li, X.; Mao, Y.; Li, L.; Wang, X.; Lin, Q. Dynamic simulation of land use change and assessment of carbon storage based on climate change scenarios at the city level: A case study of Bortala, China. *Ecol. Indic.* **2022**, *134*, 108499. [[CrossRef](#)]
25. Wang, R.; Zhao, J.; Chen, G.; Lin, Y.; Yang, A.; Cheng, J. Coupling PLUS-InVEST model for ecosystem service research in Yunnan Province, China. *Sustainability* **2022**, *15*, 271. [[CrossRef](#)]
26. Zhu, G.; Qiu, D.; Zhang, Z.; Sang, L.; Liu, Y.; Wang, L.; Zhao, K.; Ma, H.; Xu, Y.; Wan, Q. Land-use changes lead to a decrease in carbon storage in arid region, China. *Ecol. Indic.* **2021**, *127*, 107770. [[CrossRef](#)]
27. Xia, C.; Zhang, J.; Zhao, J.; Xue, F.; Li, Q.; Fang, K.; Shao, Z.; Li, S.; Zhou, J. Exploring potential of urban land-use management on carbon emissions—A case of Hangzhou, China. *Ecol. Indic.* **2023**, *146*, 109902. [[CrossRef](#)]
28. Chen, Z.; Huang, M.; Zhu, D.; Altan, O. Integrating remote sensing and a markov-FLUS model to simulate future land use changes in Hokkaido, Japan. *Remote Sens.* **2021**, *13*, 2621. [[CrossRef](#)]
29. Peng, J.; Hu, X.; Wang, X.; Meersmans, J.; Liu, Y.; Qiu, S. Simulating the impact of Grain-for-Green Programme on ecosystem services trade-offs in Northwestern Yunnan, China. *Ecosyst. Serv.* **2019**, *39*, 100998.
30. Pala, L.P.R.; Wang, Q.; Kolb, G.; Hessel, V. Steam gasification of biomass with subsequent syngas adjustment using shift reaction for syngas production: An Aspen Plus model. *Renew. Energy* **2017**, *101*, 484–492. [[CrossRef](#)]
31. Peng, Y.; Cheng, W.; Xu, X.; Song, H. Analysis and prediction of the spatiotemporal characteristics of land-use ecological risk and carbon storage in Wuhan metropolitan area. *Ecol. Indic.* **2024**, *158*, 111432. [[CrossRef](#)]
32. Zhang, J.; Zhang, C.; Dong, H.; Zhang, L.; He, S. Spatial–Temporal Change Analysis and Multi-Scenario Simulation Prediction of Land-Use Carbon Emissions in the Wuhan Urban Agglomeration, China. *Sustainability* **2023**, *15*, 11021. [[CrossRef](#)]
33. Emadi, M.; Taghizadeh-Mehrjardi, R.; Cherati, A.; Danesh, M.; Mosavi, A.; Scholten, T. Predicting and mapping of soil organic carbon using machine learning algorithms in Northern Iran. *Remote Sens.* **2020**, *12*, 2234. [[CrossRef](#)]
34. Lin, Z.; Li, M.; Zheng, Z.; Cheng, Y.; Yuan, C. Self-attention convlstm for spatiotemporal prediction. In Proceedings of the AAAI Conference on Artificial Intelligence, New York, NY, USA, 7–12 February 2020; Volume 34, pp. 11531–11538.
35. Guo, H.; Yang, C.; Liu, X.; Li, Y.; Meng, Q. Simulation evaluation of urban low-carbon competitiveness of cities within Wuhan city circle in China. *Sustain. Cities Soc.* **2018**, *42*, 688–701. [[CrossRef](#)]
36. Castro, R.; Souto, Y.M.; Ogasawara, E.; Porto, F.; Bezerra, E. Stconvs2s: Spatiotemporal convolutional sequence to sequence network for weather forecasting. *Neurocomputing* **2021**, *426*, 285–298. [[CrossRef](#)]
37. Zhou, D.-X. Theory of deep convolutional neural networks: Downsampling. *Neural Netw.* **2020**, *124*, 319–327. [[CrossRef](#)]
38. Hepburn, C.; Qi, Y.; Stern, N.; Ward, B.; Xie, C.; Zenghelis, D. Towards carbon neutrality and China’s 14th Five-Year Plan: Clean energy transition, sustainable urban development, and investment priorities. *Environ. Sci. Ecotechnol.* **2021**, *8*, 100130. [[CrossRef](#)]
39. Yao, L.; Wang, X.; Zhang, J.; Yu, X.; Zhang, S.; Li, Q. Prediction of Sea Surface Chlorophyll-a Concentrations Based on Deep Learning and Time-Series Remote Sensing Data. *Remote Sens.* **2023**, *15*, 4486. [[CrossRef](#)]
40. Shi, X.; Chen, Z.; Wang, H.; Yeung, D.-Y.; Wong, W.-K.; Woo, W.-C. Convolutional LSTM network: A machine learning approach for precipitation nowcasting. In *Advances in Neural Information Processing Systems (NIPS)*; NIPS Proceedings; MIT Press: Cambridge, MA, USA, 2015; pp. 802–810.
41. Elbasiouny, H.; El-Ramady, H.; Elbehiry, F.; Rajput, V.D.; Minkina, T.; Mandzhieva, S. Plant nutrition under climate change and soil carbon sequestration. *Sustainability* **2022**, *14*, 914. [[CrossRef](#)]

42. Zhao, M.; He, Z.; Du, J.; Chen, L.; Lin, P.; Fang, S. Assessing the effects of ecological engineering on carbon storage by linking the CA-Markov and InVEST models. *Ecol. Indic.* **2019**, *98*, 29–38. [[CrossRef](#)]
43. Balasubramanian, D.; Zhou, W.-J.; Ji, H.-L.; Grace, J.; Bai, X.-L.; Song, Q.-H.; Liu, Y.-T.; Sha, L.-Q.; Fei, X.-H.; Zhang, X. Environmental and management controls of soil carbon storage in grasslands of southwestern China. *J. Environ. Manag.* **2020**, *254*, 109810. [[CrossRef](#)]
44. Xu, Z.; Zhao, Z.; Lu, C. The contribution of land use and land cover on carbon storage in the north Tibet Plateau, China. *J. Anim. Plant Sci.* **2021**, *31*, 1598–1609.
45. Spawn, S.A.; Sullivan, C.C.; Lark, T.J.; Gibbs, H.K. Harmonized global maps of above and belowground biomass carbon density in the year 2010. *Sci. Data* **2020**, *7*, 112. [[CrossRef](#)] [[PubMed](#)]
46. Tang, L.; Ke, X.; Zhou, T.; Zheng, W.; Wang, L. Impacts of cropland expansion on carbon storage: A case study in Hubei, China. *J. Environ. Manag.* **2020**, *265*, 110515. [[CrossRef](#)] [[PubMed](#)]
47. Xiao, P.; Xu, J.; Yu, Z.; Qian, P.; Lu, M.; Ma, C. Spatiotemporal pattern differentiation and influencing factors of cultivated land use efficiency in Hubei Province under carbon emission constraints. *Sustainability* **2022**, *14*, 7042. [[CrossRef](#)]
48. Xu, L.; He, N.; Yu, G. A dataset of carbon density in Chinese terrestrial ecosystems (2010s). *China Sci. Data* **2019**, *4*, 90–96. [[CrossRef](#)]
49. Wang, Z.; Zeng, J.; Chen, W. Impact of urban expansion on carbon storage under multi-scenario simulations in Wuhan, China. *Environ. Sci. Pollut. Res.* **2022**, *29*, 45507–45526. [[CrossRef](#)]
50. Yang, J.; Huang, X. 30 m annual land cover and its dynamics in China from 1990 to 2019. *Earth Syst. Sci. Data Discuss.* **2021**, *2021*, 3907–3925. [[CrossRef](#)]
51. Xu, K.; Kong, C.; Liu, G.; Wu, C.; Deng, H.; Zhang, Y.; Zhuang, Q. Changes of urban wetlands in Wuhan, China, from 1987 to 2005. *Prog. Phys. Geogr.* **2010**, *34*, 207–220.
52. Xu, X.; Liu, J.; Zhang, S.; Li, R.; Yan, C.; Wu, S. *China's Multi-Period Land Use Land Cover Remote Sensing Monitoring Data Set (CNLUCC)*; Resource and Environment Data Cloud Platform: Beijing, China, 2018.
53. Degefu, M.A.; Argaw, M.; Feyisa, G.L.; Degefa, S. Impact of landscape dynamics and intensities on the ecological land of major cities in Ethiopia. *Environ. Syst. Res.* **2021**, *10*, 32. [[CrossRef](#)]
54. Chen, L.; Pei, S.; Liu, X.; Qiao, Q.; Liu, C. Mapping and analysing tradeoffs, synergies and losses among multiple ecosystem services across a transitional area in Beijing, China. *Ecol. Indic.* **2021**, *123*, 107329. [[CrossRef](#)]
55. Xu, Y.; Wang, L.; Fu, C.; Kosmyrna, T. A fishnet-constrained land use mix index derived from remotely sensed data. *Ann. GIS* **2017**, *23*, 303–313. [[CrossRef](#)]
56. Guo, A.; Yang, J.; Xiao, X.; Xia, J.; Jin, C.; Li, X. Influences of urban spatial form on urban heat island effects at the community level in China. *Sustain. Cities Soc.* **2020**, *53*, 101972. [[CrossRef](#)]
57. Xu, Q.; Zhu, A.-X.; Liu, J. Land-use change modeling with cellular automata using land natural evolution unit. *Catena* **2023**, *224*, 106998. [[CrossRef](#)]
58. Wang, Q.; Wang, H. An integrated approach of logistic-MCE-CA-Markov to predict the land use structure and their micro-spatial characteristics analysis in Wuhan metropolitan area, Central China. *Environ. Sci. Pollut. Res.* **2022**, *29*, 30030–30053. [[CrossRef](#)]
59. Blanton, P.; Marcus, W.A. Railroads, roads and lateral disconnection in the river landscapes of the continental United States. *Geomorphology* **2009**, *112*, 212–227. [[CrossRef](#)]
60. Muller, D.; Zeller, M. Land use dynamics in the central highlands of Vietnam: A spatial model combining village survey data with satellite imagery interpretation. *Agric. Econ.* **2002**, *27*, 333–354. [[CrossRef](#)]
61. Liu, J.; Yan, J.; Wang, L.; Huang, L.; He, H.; Liu, H. Remote sensing time series classification based on self-attention mechanism and time sequence enhancement. *Remote Sens.* **2021**, *13*, 1804. [[CrossRef](#)]
62. Zhu, L.; Song, R.; Sun, S.; Li, Y.; Hu, K. Land use/land cover change and its impact on ecosystem carbon storage in coastal areas of China from 1980 to 2050. *Ecol. Indic.* **2022**, *142*, 109178. [[CrossRef](#)]
63. Liu, X.; Wang, S.; Wu, P.; Feng, K.; Hubacek, K.; Li, X.; Sun, L. Impacts of urban expansion on terrestrial carbon storage in China. *Environ. Sci. Technol.* **2019**, *53*, 6834–6844. [[CrossRef](#)]
64. Xu, L.; Saatchi, S.S.; Yang, Y.; Yu, Y.; Pongratz, J.; Bloom, A.A.; Bowman, K.; Worden, J.; Liu, J.; Yin, Y. Changes in global terrestrial live biomass over the 21st century. *Sci. Adv.* **2021**, *7*, eabe9829. [[CrossRef](#)]

Disclaimer/Publisher's Note: The statements, opinions and data contained in all publications are solely those of the individual author(s) and contributor(s) and not of MDPI and/or the editor(s). MDPI and/or the editor(s) disclaim responsibility for any injury to people or property resulting from any ideas, methods, instructions or products referred to in the content.